Nanoscale

Radiation Damage During In-Situ Electron Microscopy of DNA-Mediated Nanoparticle Assemblies in Solution

Journal:	*Nanoscale*
Manuscript ID	NR-ART-05-2018-004087.R2
Article Type:	Paper
Date Submitted by the Author:	21-Jun-2018
Complete List of Authors:	Sutter, Peter; University of Nebraska-Lincoln, Electrical and Computer Engineering Zhang, Bo; University of Nebraska-Lincoln, Department of Mechanical and Materials Engineering Sutter, Eli; University of Nebraska-Lincoln, Department of Mechanical and Materials Engineering

Radiation Damage During *In-Situ* Electron Microscopy of DNA-Mediated Nanoparticle Assemblies in Solution

Peter Sutter,[1,*] Bo Zhang[2] and Eli Sutter[2]
[1]Department of Electrical & Computer Engineering, [2]Department of Mechanical & Materials Engineering, University of Nebraska-Lincoln, Lincoln NE 68588 (USA)

Abstract

Oligonucleotide-nanoparticle conjugates, also called programmable atom equivalents, carry promise as building blocks for self-assembled colloidal crystals, reconfigurable or stimuli responsive functional materials, as well as bio-inspired hierarchical architectures in wet environments. *In-situ* studies of the DNA-mediated self-assembly of nanoparticles have so far been limited to reciprocal space techniques. Liquid-cell electron microscopy could enable imaging such systems with high resolution in their native environment but to realize this potential, radiation damage to the oligonucleotide linkages needs to be understood and conditions for damage-free electron microscopy identified. Here, we analyze *in-situ* observations of DNA-linked two-dimensional nanoparticle arrays, along with control experiments for different oligonucleotide configurations, to identify the mechanisms of radiation damage for ordered superlattices of DNA-nanoparticle conjugates. In a biological context, the results point to new avenues for studying direct and indirect radiation effects for small ensembles of DNA in solution by tracking conjugated nanoparticles. By establishing low-dose conditions suitable for extended *in-situ* imaging of programmable atom equivalents, our work paves the way for real-space observations of DNA-mediated self-assembly processes.

*Corresponding author, e-mail: psutter@unl.edu

Introduction

Investigations of the self-assembly of colloids are driven by fundamental interest in rich phenomena found in colloidal matter that have no equivalent in conventional (atomic) solids[1-4] and by characteristics, such as widely tunable properties and the prospect of real-time reconfiguration that could support novel applications,[5] e.g., as adaptive materials. While colloidal self-assembly in general can be governed by a broad spectrum of interparticle and external forces,[2, 6] Watson-Crick base-pairing interactions between nanoparticles or micro-colloids conjugated with DNA[7] carry special promise for programmable self-assembly,[8, 9] stimuli-responsive reconfigurable clusters[10] and superlattices,[11-14] as well as anisotropically bonded crystal lattices[15] or shape-directed mesoscale and hierarchical architectures.[16, 17] Since aqueous solutions are the native medium for DNA-mediated self-assembly, capturing the underlying processes – superlattice nucleation and growth, defect formation, melting, reconfiguration, and others – requires *in-situ* measurements in liquids. Traditionally, such *in-situ* experiments have relied heavily on reciprocal space techniques such as small-angle X-ray scattering,[8, 9] but scattering or diffraction methods have limitations in probing processes and pathways that do not involve larger ordered (i.e., coherently scattering) ensembles, for instance the initial nucleation of small clusters, growth or rearrangement pathways, disorder ranging from individual defects to glassy states, etc. These restrictions can be overcome by real-space observations. Optical microscopy has been used successfully to image the self-assembly of larger DNA-functionalized micro-colloids.[4, 18-23] Extending real-time observations to DNA-mediated self-assembly of nanometer-scale particles requires microscopy in liquids at much higher spatial resolution. Liquid-cell electron

microscopy, which has been developed for *in-situ* imaging of a broad spectrum of solution-based processes including colloidal[24-27] and plasmon-mediated[28] synthesis, Brownian motion,[29] galvanic replacement,[30, 31] bio-mineralization,[32] and self-assembly of ligand-terminated nanocrystals,[33, 34] may provide real-time observations of DNA-mediated self-assembly with spatial resolution sufficient to track single nanoparticles. Observations of the motion of small DNA-linked clusters (dimers, trimers) in graphene-enclosed[35] and conventional[36] liquid cells suggest that imaging superlattices and self-assembly processes of DNA-nanoparticle conjugates in solution may be feasible, but previous work has fallen short of demonstrating *in-situ* microscopy of DNA-linked supracrystals or of the self-assembly process itself.

A key unresolved issue is the possibility that the high-energy electron beam used for imaging could perturb the sensitive DNA linkages, either directly by a number of known radiation-damage pathways to DNA[37] – induced by the primary electrons or by cascades of low-energy secondaries[38-40] – or indirectly by chemical reactions involving radicals generated by electron beam-induced radiolysis of the aqueous solution.[41-43] Previous observations showed contracting interparticle spacings in small clusters of DNA-nanoparticle conjugates at elevated electron dose rates, which were interpreted as due to enhanced dipolar interactions[36] but could instead indicate the onset of radiation damage. Time-resolved imaging experiments on larger ordered DNA-linked nanoparticle ensembles, combined with suitable control experiments, are needed to obtain a conclusive statistical analysis of dose-dependent changes in interparticle separation and of possible other effects that may accompany electron beam-induced damage to oligonucleotide linkages in solution.

Here, we report *in-situ* liquid-cell electron microscopy experiments aimed at studying the pathways of electron-beam induced damage and identifying imaging conditions that can enable extended, largely damage-free observations of DNA-mediated nanoparticle assemblies in aqueous solution. The results pave the way for the systematic use of electron microscopy for studying self-assembly and reconfiguration processes for DNA-nanoparticle conjugates in their native environment. In a broader context, our work points to new avenues for *in-situ* microscopy of radiation-induced damage to DNA in biologically relevant aqueous media. Aberration-corrected transmission electron microscopy has been used to image double-stranded DNA with sub-period resolution revealing the structure of A-DNA at the periphery of larger fiber bundles stretched between micro-pillars.[44] However, the imaging resolution achieved so far is likely insufficient to follow radiation damage mechanisms and although sufficient contrast was obtained in vacuum, direct imaging of radiation damage effects in aqueous solution, i.e., a medium with similar scattering power as the DNA itself, would be much more challenging. Other recent work has introduced closed liquid cells for irradiation of plasmid DNA in water by high-energy electrons in a scanning electron microscope.[39, 45] Whereas the irradiation occurred in bulk liquid, and thus was designed to include the full spectrum of damage mechanisms (e.g., high-energy electrons, low-energy secondaries, but also $OH^{\bullet}$ radicals and other radiolysis products in water), the damage determination was carried out *ex-situ* by gel electrophoresis. The results discussed here point to possible avenues for observing radiation damage on small ensembles or

even individual DNA-molecules in real time by tracking the motion of nanoparticles tethered by the DNA.

Results and Discussion

To study the pathways for radiation damage to DNA-mediated Au nanoparticle (NP) assemblies, synthetic oligonucleotides with sequences shown in Fig. 1 (a) were used.[8] 17 nm Au NPs were first conjugated with thiol-functionalized 28-base single-strand (SS) DNA ('particle bound DNA', see Fig. 1 (a)) and then hybridized with different SS-linker DNA strands following published procedures (see Methods).[46] DNA-Au NP conjugates linked by a functional linker with 4-nucleobase self-complementary 'sticky end' recognition sequence (shown schematically in Fig. 1 (a)) undergo self-assembly into ordered superlattice structures. Briefly, to obtain

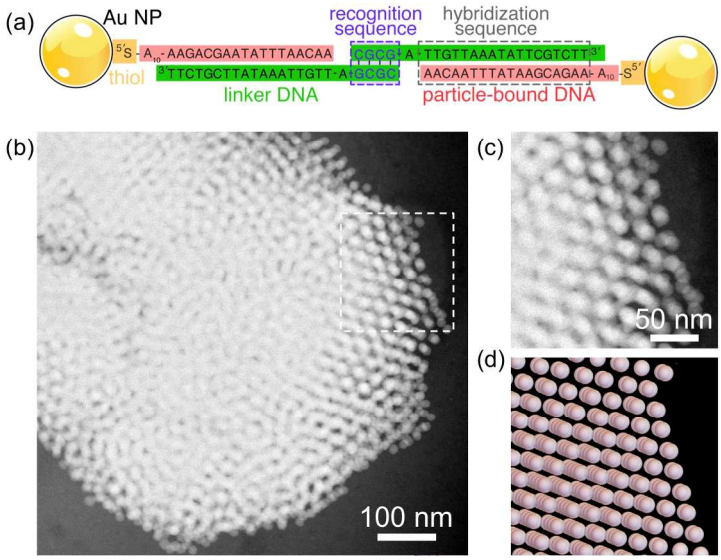

Figure 1. Superlattices of DNA-Au nanoparticle conjugates. (a) Structure of the DNA linkages used in this study. All experiments used dense shells of single-stranded (SS) particle-bound DNA anchored *via* thiol groups to Au nanoparticles (NPs). Crystallization was induced by hybridization of the particle bound DNA with SS linker DNA with a 4-base 'CGCG' recognition sequence, which defined the interparticle 'bond'. **(b)** *Ex-situ* HAADF-STEM image of a supracrystal (dry, in vacuum) with bonding provided by the DNA linkages shown in (a). **(c)** Detail of the area marked by a dashed rectangle in (b). **(d)** Ball model of a face-centered cubic (fcc) structure aligned to approximately match the particle arrangement in (c).

crystalline superlattices of linked DNA-Au NP conjugates suspended in 0.5 M NaCl, 10 mM phosphate-buffer, the suspensions were heated above the melting temperature (T_m) where the hydrogen bonds between the complementary bases in the recognition sequence are dissociated but the particle-bound and linker DNA strands remain hybridized to each other via the much longer hybridization nucleobase sequence (Fig. 1 (a)). The superlattice melting, i.e., separation of the particles due to dissociation of the recognition sequence, can readily be followed by UV-Vis spectroscopy *via* an associated change in absorption due to the re-dispersion of the DNA-Au NP conjugates in the solution (see Fig. S1).[47] We typically observed sharp melting transitions (over ~2°C), which indicates uniform loading of the Au NPs with DNA. Ordered supracrystals were then formed by slowly cooling the suspensions (at a rate of ~0.1°C/min) and annealing below T_m overnight.[8]

A high angle annular dark field scanning transmission electron microscopy (HAADF-STEM) image of a representative superlattice structure after assembly, drop cast onto a carbon film on a TEM grid and imaged dry in vacuum is shown in Fig. 1 (b). In HAADF STEM (Z-contrast imaging), the gold nanoparticles show bright contrast due to their high atomic number, Z. The DNA-linked superlattices are polycrystalline with smaller single crystalline domains (Fig. 1 (c)) that can be attributed to a face-centered cubic (fcc) arrangement of nanoparticles as seen in the ball model shown in Fig. 1(d).

For *in-situ* imaging, part of the solution (~0.1 μl) containing the self-assembled superlattices was loaded into a liquid cell with 50 μm × 50 μm ultrathin

(30 nm), electron-transparent SiN_x windows and introduced into the electron microscope.

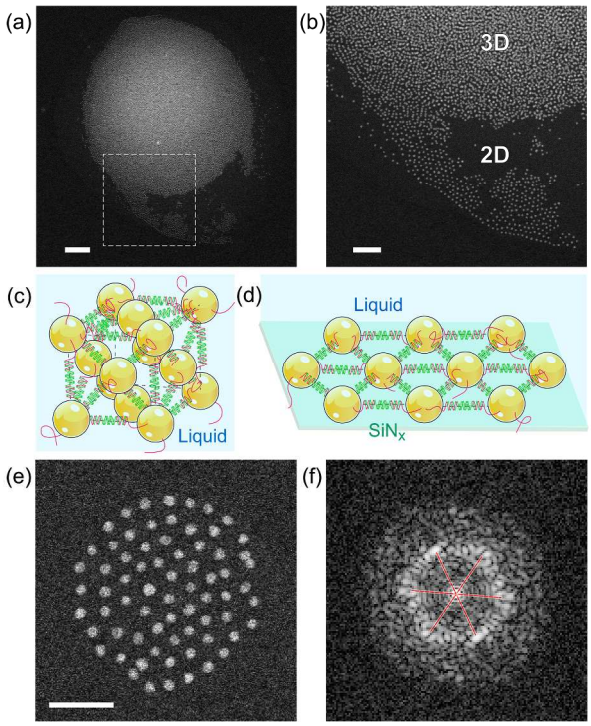

Figure 2. Liquid-cell electron microscopy of 3D and 2D DNA-linked Au nanoparticle assemblies. (a) Low-magnification *in-situ* STEM image of a large (projected diameter ~3.5 μm) DNA-Au NP assembly in 0.5 M NaCl, 10 mM phosphate-buffer aqueous solution. Scale bar: 500 nm. **(b)** Zoomed-in view of the section marked in (a), showing the transition from a 3D assembly near the center to a 2D array at the periphery. Scale bar: 200 nm. **(c)** Schematic of a DNA-mediated 3D assembly of Au nanoparticles (with assumed fcc structure, see Fig. 1) in solution. **(d)** Schematic of a close-packed 2D assembly in proximity to the SiN_x membrane of the liquid cell. **(e)** *In-situ* STEM image of a smaller isolated DNA-linked 2D assembly of 17 nm Au nanoparticles in contact with the SiN_x membrane. Scale bar: 100 nm. **(f)** Fast-Fourier transform (FFT) of the image in (e), showing the six-fold symmetry of the 2D assembly.

Representative DNA-Au NP assemblies observed by *in-situ* liquid-cell electron microscopy are shown in Fig. 2. We typically found several large three-dimensional (3D) clusters with projected diameters > 1 μm (Fig. 2 (a)). Assuming a compact shape in an unconstrained solution, enclosure in the liquid cell with a solution gap of ~400 nm caused a significant compression of these large clusters along the out-of-plane direction. This scenario is supported by frequent rupture

signatures near the cluster periphery (Fig. 2 (a), (b)). Due to their 3D structure (Fig. 2 (c)) and the applied mechanical stress, such clusters are not ideally suited for a quantitative analysis of radiation damage (Supplementary Information, Fig. S2).

Fig. 2 (b) shows an example of a different particle configuration, an ordered 2D array with large interparticle spacing, observed in the solution (here near the edge of a large 3D cluster). Such ensembles, which also frequently occurred as isolated arrays, typically contained tens to hundreds of Au NPs all of which were simultaneously in focus in STEM, implying that they were localized in the same plane normal to the optical axis, likely in proximity to one of the membranes of the liquid cell (Fig. 2 (d)). Isolated 2D assemblies (Fig. 2 (e)) greatly facilitated the real-space tracking of the configuration and interparticle spacing in self-assembled DNA-Au NP clusters. The particles in these circular 2D clusters showed a characteristic open packing of the Au NPs with ~30 nm (center-to-center) spacing (Fig. 2 (e); see also Fig. 3), and with hexagonal in-plane symmetry (Fig. 2 (f)). Electron-beam induced changes were quantified for such assemblies by following the center-to-center separation of the 17 nm Au NPs as a function of time (or electron dose) during STEM imaging. In all experiments, we ensured that the liquid cell was filled with ample solution so that the observed clusters were maintained in the liquid environment throughout.

To support the classification of electron-beam damage pathways for DNA-mediated Au NP assemblies, we carried out a series of control experiments with different DNA linkages, as shown in Fig. 3 (a): **(i)** Fully linked DNA-Au NP conjugates, bound via a functional linker with a 4-nucleobase recognition region; **(ii)**

Au NPs conjugated with particle-bound SS-DNA, which was then hybridized with 'dummy' linker DNA identical to (i) but without the recognition sequence; and **(iii)** Au NPs with particle-bound SS-DNA only, without any added linker. Previous work on DNA-mediated self-assembly suggested that the particle spacing for linked assemblies is largely determined by the cumulative length of double helix segments.[8] Damage-free *in-situ* microscopy (see below for details) allowed us to probe and statistically analyze the particle separation within 2D assemblies of several tens to hundreds of NPs for cases (i) and (ii), and within smaller multimer clusters for case (iii). The analysis of highly ordered 2D assemblies of fully linked particles, conjugated with particle-bound SS-DNA and functionalized with linker DNA with a $^{5'}$CGCG$^{3'}$ recognition sequence (Fig. 3 (a), (i)), supports the key role of the stiffer double-strand DNA segments in determining the spacing of conjugated Au NPs.[48] The measured center-to-center particle spacing of 30.0 nm (Fig. 3 (b)) is close to the expected separation for a total double helix length of (18+18+4) base pairs (30.6 nm center-to-center between NPs, or 13.6 nm DNA tether), assuming an average length of 0.34 nm per base pair in B-DNA, the most common structure found in nature comprising a right-handed double helix with about 10 base pairs per turn.[49] Au NPs conjugated with the same particle-bound SS-DNA and then transformed into mostly double-stranded (DS) DNA by hybridization with the 'dummy' linker lacking the 'sticky end' (Fig. 3 (a), (ii)) interact via non-specific forces and hence are no longer expected to lock into a 'programmed' distance. 2D assemblies of such particles still show a high degree of ordering, but crystallize with a reduced spacing compared with

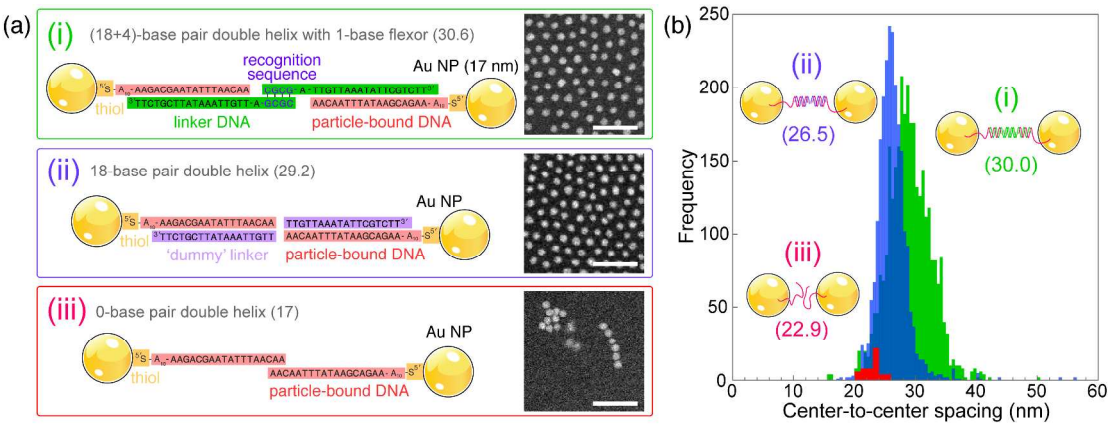

Figure 3. Analysis of the spacing of particles with different DNA termination. (a) Schematic representation of three different functionalizations: (i) Particle-bound SS-DNA and functional linker with 4-base recognition sequence; (ii) Particle-bound SS-DNA transformed into a double helix by attachment of a 'dummy' linker; and (iii) particle-bound SS-DNA only (no linker). Numbers in brackets are the predicted center-to-center separations (in nm) for 17 nm particles spaced by the total length of double helical segments (assuming a length of 0.34 nm per base pair). Images show particle configurations observed by *in-situ* electron microscopy in solution for each case. Scale bars: 100 nm. **(b)** Statistical analysis of center-to-center particle spacing from measurements by *in-situ* electron microscopy in solution. Case (iii) is based on observations of small clusters (as shown in (a)), whereas (i) and (iii) are derived from larger 2D assemblies. Numbers in brackets are measured mean center-to-center separations (in nm).

linked assemblies. A statistical analysis shows a center-to-center spacing of 26.5 nm for this case (Fig. 3 (b)), somewhat smaller than the expected separation for two 18 base-pair double helices aligned end-to-end (29.2 nm). The difference can be explained by interdigitation of the DNA strands, which would also result in an increased (non-specific) interaction and thus stabilize the unlinked assembly. Note that the width of the distribution of particle spacings (full width at half maximum FWHM = 4.2 nm) is significantly narrower for this case than for linked assemblies (FWHM = 7.2 nm). Au NPs conjugated with SS-DNA without added linker DNA (Fig. 3 (a), (iii)) no longer form large crystalline aggregates but show a tendency toward formation of few particle linear chains or smaller 2D and 3D clusters. Even though there is no DS-DNA in this case (i.e., particles are terminated by more flexible

SS-DNA only), a mean center-to-center NP spacing of ~23 nm is maintained (Fig. 3 (b)), consistent with steric repulsion between folded SS-DNA or wrapping/coiling of the strands around the NPs.[50, 51]

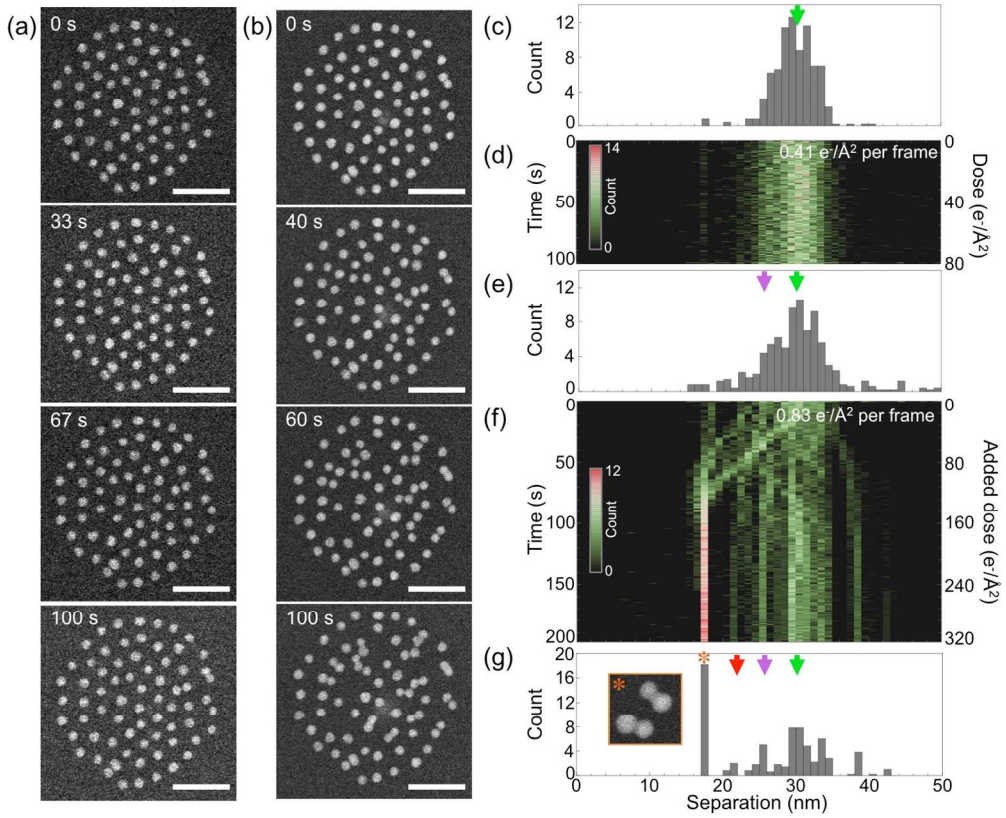

Figure 4. Electron-beam damage to DNA visualized in 2D assemblies. (a) Time-lapse sequence of STEM images (primary energy: 200 keV), showing a 2D assembly in the initial state (minimal electron dose), and after 33 s, 67 s, and 100 s of low-dose STEM imaging (t_{img} = 0.52 s). Scale bars: 100 nm. **(b)** Time-lapse sequence of STEM images of the same 2D assembly at higher dose rate, after additional 40 s, 60 s, and 100 s of STEM imaging. Scale bars: 100 nm. Note the progressive decrease in interparticle spacing, which ultimately leads to the formation of several closely spaced 'dimer' pairs. **(c)** Initial histogram of center-to-center particle spacing (t = 0 in (a)). **(d)** Density plot of the time evolution of the particle spacing histogram from t = 0 to 100 s of low-dose imaging (corresponding to image sequence (a)) Each 'slice' at constant time corresponds to a full histogram of the distribution of center-to-center particle spacing, similar to that shown in (c)) but with the counts represented by colors according to the scale shown near the left edge of the plot. **(e)** Histogram of center-to-center particle spacing at t = 100 s in (a). **(f)** Density plot of the time evolution of the particle spacing histogram from t = 0 to 200 s of higher-dose imaging (corresponding to image sequence (b)). Note the two distinct transitions toward closely spaced particle pairs ('dimers'), for particles initially spaced at ~26 nm and ~30 nm, respectively. **(g)** Histogram of center-to-center particle spacing at t = 200 s in (b). The inset shows two representative 'dimers' with center-to-center spacing *d* ~ 17 nm. For electron dose information, see Table S1.

The above analysis of three situations – DNA linked NPs, NPs with 'dummy' linker complementary to the base sequence of the particle-bound DNA, and NPs with particle-bound SS-DNA only – can serve as a benchmark reference for *in-situ* experiments on electron-beam damage of DNA-mediated assemblies, starting from 2D assemblies of DNA-NP conjugates interacting via functional linker DNA with recognition sequence (Fig. 3 (a), (i)). In STEM imaging, a small focused probe beam (beam size ~2 Å) is continuously scanned across the field of view. Detailed information about the scan pattern and the derived distribution of the electron dose is given in the Supplementary Information. The electron dose per image frame is determined by several variables, including the electron beam current ($\mathbf{I_e}$), the physical image size and pixel count, and the acquisition time per image frame ($\mathbf{t_{img}}$). By proper choice of these parameters, very low electron doses can be achieved. Importantly, during the scan the high-energy electron beam is projected into an 'exposure track' whose width approximately equals the beam diameter, and most of the field of view experiences no direct electron exposure (see Fig. S5, Fig. S6). Frame-to-frame statistical variations in the location of this exposure track distribute the electron dose across different parts of the sample in consecutive image frames, thus further reducing the cumulative dose in longer imaging time-series. Hence, where cumulative doses are reported, calculated as (dose per image frame projected into the exposure track) × (cumulative time/$\mathbf{t_{img}}$), they represent upper bounds (worst cases) and likely overestimate the actual dose. A summary of all experimental parameters and of the derived *dose per image frame projected into the exposure track* for all experiments

reported here is given in Supplementary Table S1. Stated dose rates have been calculated as (dose per image projected into the exposure track)/$\mathbf{t_{img}}$.

In the experiment shown in Fig. 4, continuous scanning of a DNA-linked 2D Au NP array by STEM at a rate of 2 frames/s ($\mathbf{t_{img}}$ = 0.52 s) was used to image and simultaneously expose the assembly to high-energy electrons at a controlled rate. At a fixed primary energy of 200 keV, two types of conditions at different electron dose per image frame were used: during the initial 100 s, a low local dose of 0.41 $e^-/Å^2$ per image (dose rate 0.79 $e^-/(Å^2 \cdot s)$ for the exposure track) was maintained – see the image sequence in Fig. 4 (a), as well as corresponding density plots of the evolution of center-to-center particle separation (Fig. 4 (d)) and the initial and final separation histograms in Figs. 4 (c) and (e), respectively. For the following 200 s the assembly was imaged/exposed at a higher dose of 0.83 $e^-/Å^2$ per image (dose rate 1.60 $e^-/(Å^2 \cdot s)$). The corresponding image sequence is shown in Fig. 4 (b); density plots of the time-dependent interparticle spacing and separation histograms are given in Figs. 4 (e)-(g).

The response of the 2D DNA-Au NP assembly to low-dose imaging is quite subtle. Initially, the particles arranged in a hexagonal array are mostly widely spaced with a mean center-to-center separation of 30 nm (Fig. 4 (c)), characteristic of DNA-linked nanoparticles (Fig. 3 (b), (i)). There is only one closely spaced pair of particles, with a second one generated early during the electron exposure. With increasing exposure time, the separation histogram shows the peak at 30 nm decreasing while a second maximum develops at smaller spacing (Fig. 4 (d)). After 100 s exposure, part of the assembly shows a particle spacing of ~26 nm (Fig. 4 (e)), close to the separation of DNA-Au NP conjugates hybridized with the non-functional ('dummy')

linker. We thus conclude that the initial pathway of electron beam damage in aqueous solution involves the dissociation of hydrogen bonds between DNA base pairs. Given the relative lengths of the hybridization sequence (18 base pairs) and recognition sequence (4 base pairs), the observed net effect is a dissociation of the recognition base pairs for a sizable fraction of the particles in the assembly, which essentially convert to a state corresponding to Fig. 3 (a), (ii) ('dummy' linker) in our control experiments.

The following imaging and exposure at increased beam current induces larger, more rapidly developing changes (Fig. 4 (f)). Within ~80 s of additional exposure a new steady state develops in which only a minority of nearest neighbor pairs still show the initial 30 nm spacing whereas a large population of 'dimers' has formed in which pairs of particles are nearly in direct contact with each other (separation ~17 nm). In addition discrete peaks appear corresponding to separations of 26 nm and 22 nm, respectively, close to those found for 'dummy' linker hybridized and unlinked DNA-NP conjugates (Fig. 3). Note also the emergence of peaks at larger spacings, which represent the increased separation between pairs of closely spaced particles.

The time-dependent separation histogram (Fig. 4 (f)) provides information about the transition from the initial to the final distributions. In particular, we find two distinct transitions toward closely spaced particles ('dimers'). The first one affects particles with ~26 nm spacing, i.e., with already dissociated recognition sequence following the low dose electron exposure. Such particle pairs move progressively closer and become 'dimers' after ~50 s of higher-dose imaging. Pairs of linked particles with 30 nm initial spacing approach each other at roughly the same rate and

become ‘dimers’ after ~75 s of higher-dose electron exposure. 2D arrays of DNA-Au NP conjugates hybridized to the ‘dummy’ linker show a similar formation of closely spaced ‘dimers’ during electron irradiation (Fig. S3), but their evolution is much more rapid even at low dose rates, i.e., they appear more sensitive to radiation damage than the fully linked assemblies shown in Fig. 4. The observed continuous changes in interparticle separation illustrate that the particles are sufficiently mobile to respond to radiation damage to the DNA tether despite being located near one of the SiN_x membranes of the liquid cell. While our experiments are not yet providing direct evidence for the mechanism underlying this pairwise approach, the observed behavior is consistent with a shortening of the DNA by either single- or double-strand breakage events.[39] Previous work showed that such events are disproportionally triggered by low-energy electrons,[38-40] and implicated Au nanoparticles as efficient scatterers that can transform the high-energy primary electrons into cascades of low-energy secondaries.[52, 53] Radicals produced by radiolysis of the aqueous solution are likely involved in the base-pair dissociation processes that give rise to the discrete peaks corresponding to ‘dummy’ linked (26 nm spacing) and unlinked (22 nm) particles.[42] While radiation damage in 3D clusters of DNA-linked Au NPs (Fig. 1, Fig. 2 (a)) is more difficult to assess quantitatively, the same characteristic behavior is observed in 3D assemblies as for 2D ensembles under extended irradiation, notably a repositioning of the initially equidistant NPs to form small clusters of closely-spaced particles, which in turn are separated from each other by larger gaps (Fig. S2).

At late stages, electron irradiation can cause extensive damage, culminating in the dissociation of the entire remaining DNA conjugate and ultimately cleavage of the

thiol group from the surface of the Au NPs. The resulting processes involving the now unconjugated and deprotected Au NPs are illustrated in Fig. 5 (a). At the beginning of this image sequence, the particles are already closely spaced due to the effects described above, but they remain monodisperse with 17 nm average diameter. Additional electron exposure causes a distinct increase in the average particle size and reduction in the number of particles, which occur via two different processes: (i) Coalescence of closely spaced particles (Fig. 5 (b)); and (ii) jumps of nanoparticles

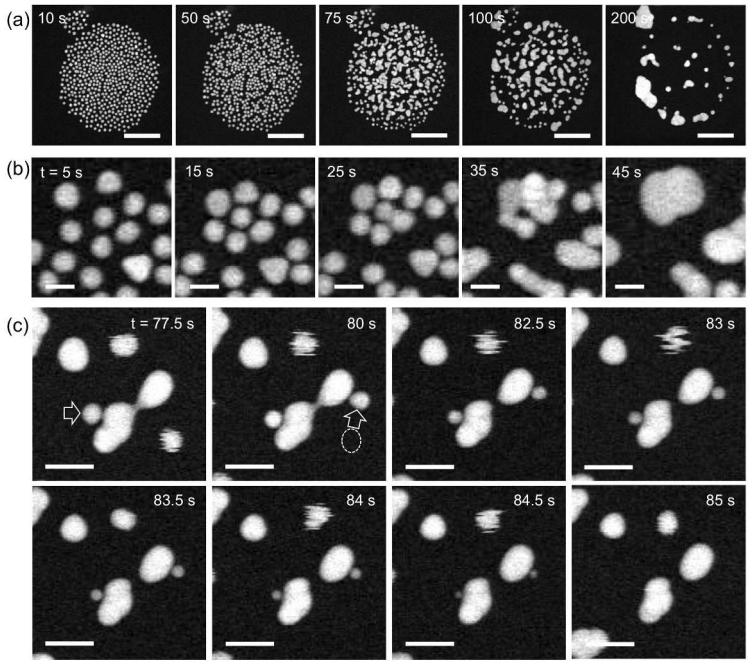

Figure 5. Advanced stages of electron damage to DNA-mediated 2D assemblies. (a) Time-lapse series of STEM images of a large 2D nanoparticle assembly, showing the evolution from t = 10 s to 200 s exposure to 200 keV electrons (electron dose rate: ~51 e^- /($Å^2$·s). Note the rapid increase in average particle size beginning at t ~ 50 s, which ultimately leads to the formation of large Au clusters. Scale bars: 200 nm. **Mechanisms of particle size increase: (b)** Time-lapse series of STEM images (excerpt from (a)) showing the coalescence of Au NPs. Scale bars: 20 nm. **(c)** Time-lapse series of STEM images (excerpt from (a)) showing jumps to contact (arrows), followed by Ostwald ripening with surface diffusion as the mass transport mechanism. Scale bars: 50 nm. For electron dose information, see Table S1.

that bring them into close contact with each other (indicated with arrows in Fig. 5 (c)), followed by Ostwald ripening in which the smaller particles shrink and disappear by

atomic detachment and the material gets incorporated via surface mass transport in the larger particles which grow at their expense (Fig. 5 (c), see also Fig. S4). The coalescence and Ostwald ripening are probably due to the damage of the DNA at these late stages which leaves the gold nanoparticles unprotected and creates a

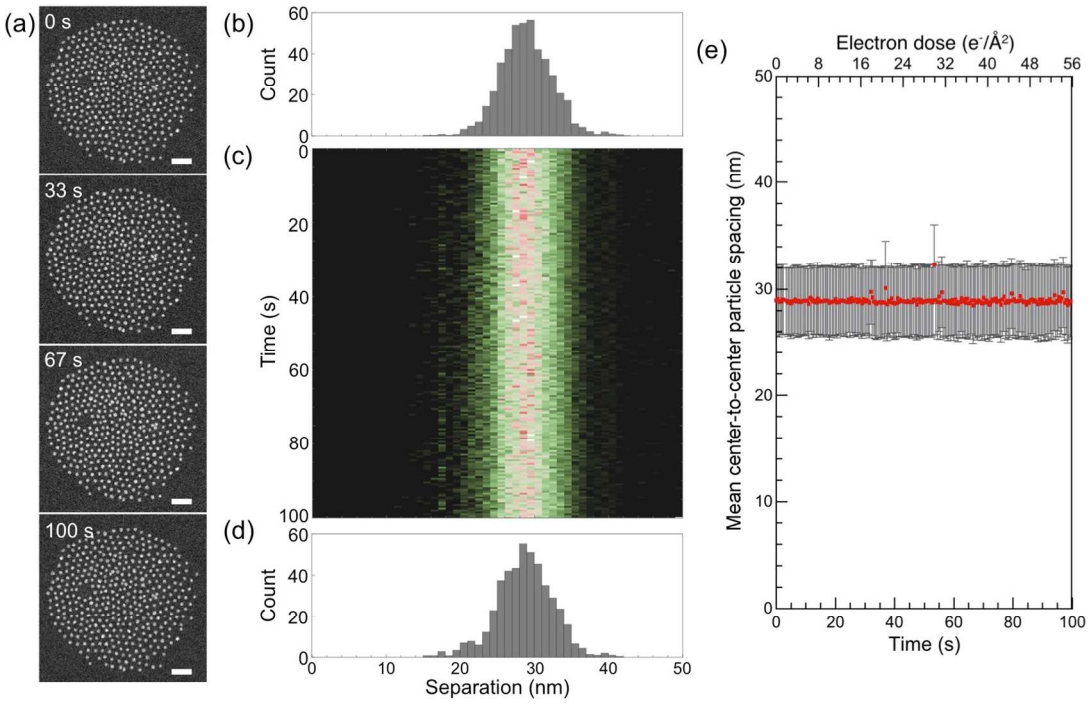

Figure 6. Damage-free *in-situ* STEM imaging of DNA-mediated 2D assemblies in solution. (a) Time-lapse sequence of STEM images (primary energy: 200 keV), showing a 2D assembly in the initial state (minimal electron dose), and after 33 s, 67 s, and 100 s of low-dose STEM imaging ($\mathbf{t_{img}}$ = 0.52 s, dose rate 0.56 $e^-/(Å^2 \cdot s)$ into the exposure track). Note the ample image contrast sufficient to track individual particles, and the absence of noticeable changes in interparticle spacing over the entire observation period. Scale bars: 100 nm. **(b)** Initial histogram of center-to-center particle separation (corresponding to t = 0 in (a)), with mean center-to-center spacing $\langle d \rangle$ = 29.6 nm. **(c)** Density plot of the time dependent particle separation histograms during continuous low-dose STEM imaging for a total duration of 100 s. Each 'slice' at constant time corresponds to a histogram of the distribution of center-to-center particle spacing, similar to that shown in (b)) but with the counts represented by colors according to the scale shown near the left edge of the plot. **(d)** Final histogram of center-to-center particle separation after 100 s exposure to 200 keV electrons in STEM (t = 100 s in (a)), with mean center-to-center spacing $\langle d \rangle$ = 29.3 nm. **(e)** Evolution of the mean center-to-center particle spacing with elapsed time. Error bars represent ± 1σ (standard deviation) of the sets of measured particle spacing at each time. Note that the given cumulative dose (calculated as (dose per image projected into the exposure track) × (cumulative time/$\mathbf{t_{img}}$)) likely overestimates the actual dose (see comment in the text above). For electron dose information, see Table S1.

chemical potential difference driving mass transport between particles of different sizes. Under the conditions used here (phosphate buffered aqueous solution, 0.5 M NaCl), the dissolution of Au NPs observed in previous work at high salinity and low pH was not detected.[54]

Based on the findings above, we identified imaging conditions that allow extended, essentially damage-free *in-situ* microscopy of DNA-mediated NP assemblies in their native solution environment. An example of such an image sequence, obtained at an exposure track dose below 0.3 $e^-/Å^2$ per frame is shown in Fig. 6. Here, a large 2D array containing ~400 DNA-linked Au NPs remains unchanged with minimal broadening or shift of the distribution of center-to-center particle separations during an observation period of 100 s at 2 frames/s ($\mathbf{t_{img}}$ = 0.52 s). This implies an absence of the telltale reduction of the interparticle spacing, which our experiments identified as the key characteristic of electron-beam damage to the DNA linkages (Fig. 4).

Conclusions

The identification of damage-free low-dose imaging conditions in HAADF-STEM implies that *in-situ* microscopy can be a viable approach for real-space imaging of DNA-mediated self-assembly, with particular impact on understanding processes that are not amenable to the conventional *in-situ* diffraction methods and which cannot be probed by *ex-situ* measurements. Important examples of such processes are the initial nucleation and growth of self-assembled superlattices; the onset of melting; defect formation, e.g., the generation of point- or extended defects due to the creation of vacancies, the trapping of particles in metastable (interstitial) positions, coordination errors, stacking faults, etc.; jamming and the formation of

disordered (glassy) structures; and the reconfiguration of DNA-mediated assemblies in response to externally applied stimuli. Further adaptation of the experimental protocol, e.g., by imaging at intervals that are commensurate with the kinetics of the targeted processes or by adding appropriate scavengers to capture radiolysis products (e.g., $OH^{\bullet}$ radicals)[30] implicated in the initial electron beam induced dissociation of DNA base pairs in the linker recognition sequence, can ensure that the dose is further reduced so as to extend the observation time from > 100 s of continuous imaging at 2 frames/s, as shown here, to much longer times of the order of minutes to hours, i.e., intervals that are sufficiently long to capture slower processes, such as superlattice reconfiguration[11-14] or exotic phase behavior of DNA-NP assemblies.[4]

Experimental

Citrate-capped Au nanoparticles (Pelco NanoXact and BioPure) with 20 nm nominal diameter (17 nm actual diameter, as measured by electron microscopy) and concentration of 1.3×10^{11} particles/mL were used as starting material. Oligonucleotides (*Particle-bound*: 5'-thiol modifier-A10-AAGACGAATATTTAACAA-3'; *Functional linker*: 3'-TTCTGCTTATAAATTGTT-A-GCGC-5'; *'Dummy' linker*: 3'-TTCTGCTTATAAATTGTT-5') were purchased from Integrated DNA Technologies. The functionalization of the Au nanoparticles was performed following the protocol described in Refs. [46] and [55]. UV-Vis spectroscopy and melting curves of the Au nanoparticle assemblies were measured using a Perkin Elmer Lambda 265 spectrophotometer equipped with a precision Peltier temperature controller with 0.1°C temperature stability. Real-time (S)TEM experiments were carried out in a

dedicated specimen holder (Hummingbird Scientific) using liquid cells consisting of two 30 nm thick SiN_x membrane windows with 50 × 50 μm^2 window area. The spacing between the windows was controlled using 100 nm and 200 nm SiO_2 spacers. Bowing of the thin membranes allows a continuous range of liquid thicknesses to be established within the same cell.[25] STEM imaging was performed in a FEI Talos F200X microscope operated at 200 kV, selected to provide a compromise between beam energies that minimize knock-on damage (low energy regime) and conditions that lead to reduced ionization damage or radiolysis (higher primary energies).[56] STEM imaging was performed with ~2 Å probe size and the beam current was varied in the range between 1 – 90 pA, measured in vacuum before introduction of the liquid cell. Typical conditions for the acquisition of time lapse image series were 512 × 512 pixels, and pixel dwell times of 2 μs ($\mathbf{t_{img}}$ = 0.52 s/frame) or 4 μs ($\mathbf{t_{img}}$ = 1.05 s/frame). The electron doses were calculated based on the scan pattern in STEM according to the procedure described in the Supplementary Information (Supplementary Note 1). Detailed information about the dose calculation for each experiment reported here (Figs. 4, 5, 6; Supplementary Figs. S2, S3, S4) is given in the Supplementary Information, Table S1. Low-dose imaging is facilitated by the fact that only a small portion of the field of view is directly exposed to the focused scanning electron probe (exposure track). In time series across many image frames, scan non-idealities such as deflection coil hysteresis, fly-back distortion, or drift cause random shifts of the exposure track from one image to the next so that the dose over longer times (> 1 frame) is effectively averaged over a large area, which significantly reduces the cumulative electron dose in each image area (i.e., the electron dose in microscopic

areas is not simply additive for consecutive scans). The analysis of the observed assemblies was performed in the software package *ImageJ*,[57] using built-in threshold and particle analysis (centroid coordinates) functions. Sequences of grayscale STEM images were segmented into features of interest and background using the global thresholding function, which resulted in a binary representation of well-separated particles (white) on a black background. The centroid coordinates of each particle were then determined for each image frame using the corresponding particle analysis function in *ImageJ*. The error of this process of determining the center coordinates for all particles is estimated to be below 1 pixel (which typically corresponds to ~1 nm) in both x- and y-directions. Finally, the *"NND"* plugin was used to compute nearest-neighbor particle spacings from the sets of centroid particle coordinates. Histograms of particle sizes and center-to-center separations (Figs. 3, 4, 6; Figs. S3, S4) were generated in *Mathematica*.

Conflicts of Interest

There are no conflicts to declare.

Supporting Information

Supporting Figures S1 to S6: UV-Vis spectroscopy of DNA-Au NP superlattice melting and crystallization; radiation damage in 3D DNA-mediated Au nanoparticle assemblies; evolution of 2D assemblies of 'dummy' linker terminated particles; analysis of advanced stages of electron damage to DNA-mediated 2D assemblies; scan pattern in STEM; distribution of areas exposed to the scanning electron beam (exposure track). *Supporting Note 1:* Calculation of the effective electron dose. *Table S1:* Summary of experimental parameters and electron dose per frame for all reported experiments/figures (PDF).

Acknowledgements

This material is based upon work supported by the U. S. Army Research Laboratory and the U.S. Army Research Office under grant number W911NF-17-1-0141. The authors acknowledge seed funding from the Nebraska Public Power District through

the Nebraska Center for Energy Sciences Research, and technical support by Q. Wu and S. Sutter.

References

1. V. N. Manoharan, *Science*, 2015, **349**, 1253751.
2. C. A. Silvera Batista, R. G. Larson and N. A. Kotov, *Science*, 2015, **350**, 1242477.
3. D. Frenkel, *Nature Materials*, 2014, **14**, 9.
4. W. B. Rogers and V. N. Manoharan, *Science*, 2015, **347**, 639-642.
5. Z. Nie, A. Petukhova and E. Kumacheva, *Nature Nanotechnology*, 2009, **5**, 15.
6. Y. Min, M. Akbulut, K. Kristiansen, Y. Golan and J. Israelachvili, *Nature Materials*, 2008, **7**, 527.
7. C. A. Mirkin, R. L. Letsinger, R. C. Mucic and J. J. Storhoff, *Nature*, 1996, **382**, 607.
8. S. Y. Park, A. K. R. Lytton-Jean, B. Lee, S. Weigand, G. C. Schatz and C. A. Mirkin, *Nature*, 2008, **451**, 553.
9. D. Nykypanchuk, M. M. Maye, D. van der Lelie and O. Gang, *Nature*, 2008, **451**, 549.
10. D. S. Sebba, J. J. Mock, D. R. Smith, T. H. LaBean and A. A. Lazarides, *Nano Letters*, 2008, **8**, 1803-1808.
11. Y. Zhang, S. Pal, B. Srinivasan, T. Vo, S. Kumar and O. Gang, *Nature Materials*, 2015, **14**, 840.
12. M. M. Maye, M. T. Kumara, D. Nykypanchuk, W. B. Sherman and O. Gang, *Nature Nanotechnology*, 2009, **5**, 116.
13. Y. Kim, R. J. Macfarlane, M. R. Jones and C. A. Mirkin, *Science*, 2016, **351**, 579-582.
14. J. A. Mason, C. R. Laramy, C.-T. Lai, M. N. O'Brien, Q.-Y. Lin, V. P. Dravid, G. C. Schatz and C. A. Mirkin, *Journal of the American Chemical Society*, 2016, **138**, 8722-8725.
15. W. Liu, M. Tagawa, H. L. Xin, T. Wang, H. Emamy, H. Li, K. G. Yager, F. W. Starr, A. V. Tkachenko and O. Gang, *Science*, 2016, **351**, 582-586.
16. Z. Zeravcic, V. N. Manoharan and M. P. Brenner, *Proceedings of the National Academy of Sciences*, 2014, **111**, 15918-15923.
17. J. D. Halverson and A. V. Tkachenko, *Physical Review E*, 2013, **87**, 062310.
18. A. J. Kim, P. L. Biancaniello and J. C. Crocker, *Langmuir*, 2006, **22**, 1991-2001.
19. M.-P. Valignat, O. Theodoly, J. C. Crocker, W. B. Russel and P. M. Chaikin, *Proceedings of the National Academy of Sciences of the United States of America*, 2005, **102**, 4225-4229.
20. V. T. Milam, A. L. Hiddessen, J. C. Crocker, D. J. Graves and D. A. Hammer, *Langmuir*, 2003, **19**, 10317-10323.
21. C. M. Soto, A. Srinivasan and B. R. Ratna, *Journal of the American Chemical Society*, 2002, **124**, 8508-8509.
22. Y. Wang, Y. Wang, X. Zheng, É. Ducrot, J. S. Yodh, M. Weck and D. J. Pine, *Nature Communications*, 2015, **6**, 7253.
23. P. H. Rogers, E. Michel, C. A. Bauer, S. Vanderet, D. Hansen, B. K. Roberts, A. Calvez, J. B. Crews, K. O. Lau, A. Wood, D. J. Pine and P. V. Schwartz, *Langmuir*, 2005, **21**, 5562-5569.
24. T. J. Woehl, J. E. Evans, I. Arslan, W. D. Ristenpart and N. D. Browning, *ACS Nano*, 2012, **6**, 8599-8610.
25. K. L. Jungjohann, S. Bliznakov, P. W. Sutter, E. A. Stach and E. A. Sutter, *Nano Letters*, 2013, **13**, 2964-2970.
26. H. Zheng, R. K. Smith, Y.-w. Jun, C. Kisielowski, U. Dahmen and A. P. Alivisatos, *Science*, 2009, **324**, 1309-1312.

27. E. A. Sutter and P. W. Sutter, *Journal of the American Chemical Society*, 2014, **136**, 16865-16870.
28. P. Sutter, Y. Li, C. Argyropoulos and E. Sutter, *Journal of the American Chemical Society*, 2017, **139**, 6771-6776.
29. H. Zheng, S. A. Claridge, A. M. Minor, A. P. Alivisatos and U. Dahmen, *Nano Letters*, 2009, **9**, 2460-2465.
30. E. Sutter, K. Jungjohann, S. Bliznakov, A. Courty, E. Maisonhaute, S. Tenney and P. Sutter, *Nature Communications*, 2014, **5**, 4946.
31. E. A. Sutter and P. W. Sutter, *Nanoscale*, 2017, **9**, 1271-1278.
32. P. J. M. Smeets, K. R. Cho, R. G. E. Kempen, N. A. J. M. Sommerdijk and J. J. De Yoreo, *Nature Materials*, 2015, **14**, 394.
33. E. Sutter, P. Sutter, A. V. Tkachenko, R. Krahne, J. de Graaf, M. Arciniegas and L. Manna, *Nature Communications*, 2016, **7**, 11213.
34. J. Park, H. Zheng, W. C. Lee, P. L. Geissler, E. Rabani and A. P. Alivisatos, *ACS Nano*, 2012, **6**, 2078-2085.
35. Q. Chen, J. M. Smith, J. Park, K. Kim, D. Ho, H. I. Rasool, A. Zettl and A. P. Alivisatos, *Nano Letters*, 2013, **13**, 4556-4561.
36. S. Keskin, S. Besztejan, G. Kassier, S. Manz, R. Bücker, S. Riekeberg, H. K. Trieu, A. Rentmeister and R. J. D. Miller, *The Journal of Physical Chemistry Letters*, 2015, **6**, 4487-4492.
37. J. F. Ward, in *Progress in Nucleic Acid Research and Molecular Biology*, eds. W. E. Cohn and K. Moldave, Academic Press, 1988, vol. 35, pp. 95-125.
38. B. Boudaïffa, P. Cloutier, D. Hunting, M. A. Huels and L. Sanche, *Science*, 2000, **287**, 1658-1660.
39. M. B. Hahn, S. Meyer, M.-A. Schroter, H. Seitz, H.-J. Kunte, T. Solomun and H. Sturm, *Physical Chemistry Chemical Physics*, 2017, **19**, 1798-1805.
40. W. Chen, S. Chen, Y. Dong, P. Cloutier, Y. Zheng and L. Sanche, *Physical Chemistry Chemical Physics*, 2016, **18**, 32762-32771.
41. S. Steenken, *Chemical Reviews*, 1989, **89**, 503-520.
42. J. Cadet, T. Delatour, T. Douki, D. Gasparutto, J.-P. Pouget, J.-L. Ravanat and S. Sauvaigo, *Mutation Research/Fundamental and Molecular Mechanisms of Mutagenesis*, 1999, **424**, 9-21.
43. M. Dizdaroglu, P. Jaruga, M. Birincioglu and H. Rodriguez, *Free Radical Biology and Medicine*, 2002, **32**, 1102-1115.
44. M. Marini, A. Falqui, M. Moretti, T. Limongi, M. Allione, A. Genovese, S. Lopatin, L. Tirinato, G. Das, B. Torre, A. Giugni, F. Gentile, P. Candeloro and E. Di Fabrizio, *Science Advances*, 2015, **1**, e1500734.
45. M. B. Hahn, S. Meyer, H.-J. Kunte, T. Solomun and H. Sturm, *Physical Review E*, 2017, **95**, 052419.
46. H. D. Hill and C. A. Mirkin, *Nature Protocols*, 2006, **1**, 324.
47. R. C. Mucic, J. J. Storhoff, C. A. Mirkin and R. L. Letsinger, *Journal of the American Chemical Society*, 1998, **120**, 12674-12675.
48. R. S. Mathew-Fenn, R. Das and P. A. B. Harbury, *Science*, 2008, **322**, 446-449.
49. M. Levitt, *Proceedings of the National Academy of Sciences*, 1978, **75**, 640-644.
50. E. M. Nelson and L. J. Rothberg, *Langmuir*, 2011, **27**, 1770-1777.
51. X. Zhang, B. Liu, N. Dave, M. R. Servos and J. Liu, *Langmuir*, 2012, **28**, 17053-17060.
52. Y. Zheng, D. J. Hunting, P. Ayotte and L. Sanche, *Radiation Research*, 2008, **169**, 19-27.
53. X. Fangxing, Z. Yi, C. Pierre, H. Yunhui, H. Darel and S. Léon, *Nanotechnology*, 2011, **22**, 465101.
54. J. Hermannsdorfer, N. de Jonge and A. Verch, *Chemical Communications*, 2015, **51**, 16393-16396.

55. S. J. Hurst, A. K. R. Lytton-Jean and C. A. Mirkin, *Analytical Chemistry*, 2006, **78**, 8313-8318.
56. D. B. Williams and C. B. Carter, *Transmission Electron Microscopy*, Springer US, 2009.
57. C. A. Schneider, W. S. Rasband and K. W. Eliceiri, *Nat Meth*, 2012, **9**, 671-675.

Summary Graphic